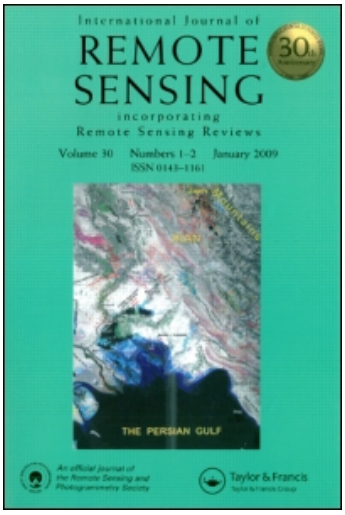

International Journal of Remote Sensing
Publication details, including instructions for authors and subscription information:
http://www.informaworld.com/smpp/title~content=t713722504

Relationship between LiDAR-derived forest canopy height and Landsat images

Cristina Pascual [a]; Antonio García-Abril [a]; Warren B. Cohen [b];Susana Martín-Fernández [a]
[a] E.T.S.I. Montes, Technical University of Madrid (UPM), Ciudad Universitaria s.n., Madrid, Spain [b] Forestry Sciences Laboratory, Pacific Northwest Research Station, USDA Forest Service, Corvallis, OR, USA

Online publication date: 30 March 2010

To cite this Article Pascual, Cristina , García-Abril, Antonio , Cohen, Warren B. andMartín-Fernández, Susana(2010) 'Relationship between LiDAR-derived forest canopy height and Landsat images', International Journal of Remote Sensing, 31: 5, 1261 — 1280
To link to this Article: DOI: 10.1080/01431160903380656
URL: http://dx.doi.org/10.1080/01431160903380656

International Journal of Remote Sensing
Vol. 31, No. 5, 10 March 2010, 1261–1280

Taylor & Francis
Taylor & Francis Group

Relationship between LiDAR-derived forest canopy height and Landsat images

CRISTINA PASCUAL*†, ANTONIO GARCÍA-ABRIL†,
WARREN B. COHEN‡ and SUSANA MARTÍN-FERNÁNDEZ†

†E.T.S.I. Montes, Technical University of Madrid (UPM), Ciudad Universitaria s.n., 28040 Madrid, Spain

‡Forestry Sciences Laboratory, Pacific Northwest Research Station, USDA Forest Service, 3200 SW Jefferson Way, Corvallis, OR 97311, USA

The mean and standard deviation (SD) of light detection and ranging (LiDAR)-derived canopy height are related to forest structure. However, LiDAR data typically cover a limited area and have a high economic cost compared with satellite optical imagery. Optical images may be required to extrapolate LiDAR height measurements across a broad landscape. Different spectral indices were obtained from three Landsat scenes. The mean, median, SD and coefficient of variation (CV) of LiDAR canopy height measurements were calculated in 30-m square blocks corresponding with Landsat Enhanced Thematic Mapper Plus (ETM+) pixels. Correlation and forward stepwise regression analysis was applied to these data sets. Mean and median LiDAR height versus normalized difference vegetation index (NDVI), normalized difference moisture index (NDMI), normalized burn ratio (NBR) and wetness Tasseled Cap showed the best correlation coefficients (R^2 ranging between –0.62 and –0.76). Nineteen regression models were obtained ($R^2 = 0.65$–0.70). These results show that LiDAR-derived canopy height may be associated with Landsat spectral indices. This approach is of interest in sustainable forest management, although further research is required to improve accuracy.

1. Introduction

Forest canopy structure and forest stand attributes are increasingly recognized as being of theoretical and practical importance in understanding and managing forest ecosystems. As the primary attribute of vertical structure, canopy height is essential information for many forest management activities and is a crucial parameter in models of ecosystem processes (Franklin *et al*. 2002, Sexton *et al*. 2009). Forest studies require a great deal of field effort and time. Consequently, remote sensing techniques and statistical modelling have been advanced to assist in forest surveys.

In the past decade, light detection and ranging (LiDAR) data have proved to be extremely useful in the three-dimensional (3D) characterization of forest canopy and the estimation of forest attributes (Lefsky *et al*. 2002, Hyyppa *et al*. 2008). Specifically, mean and standard deviation (SD) of LiDAR-derived height can be used to synthesize the 3D distribution of canopy structure. Zimble *et al*. (2003) used LiDAR-derived tree height variances to distinguish between single-storey and multi-storey forest classes. Lefsky *et al*. (2005a) showed that mean height and height variability derived from LiDAR data are strongly related to stand structure and they consider

*Corresponding author. Email: c.pascual@upm.es

International Journal of Remote Sensing
ISSN 0143-1161 print/ISSN 1366-5901 online
http://www.tandf.co.uk/journals
DOI: 10.1080/01431160903380656

these variables to represent the same kind of enhancement that the Tasseled Cap indices (Crist and Cicone 1984) represent for optical remote sensing. Pascual *et al.* (2008) found that mean, median and SD of canopy height derived from LiDAR could be used to distinguish horizontally heterogeneous forest structure types in *Pinus sylvestris* L. stands.

Laser scanners provide detailed information on the vertical distribution of forest canopy structure (Hyyppa *et al.* 2008), but over a limited area and at a high economic cost. Landsat data provide useful structural information in the horizontal plane and are much more readily available (Cohen and Spies 1992). Therefore, the integration of optical remote sensing imagery and LiDAR data provides opportunities to fully characterize forest canopy attributes and dynamics over large areas (Wulder *et al.* 2007). There have been several studies on this subject.

Hudak *et al.* (2002) developed spatial extrapolation of LiDAR data over Landsat Enhanced Thematic Mapper Plus (ETM+) images. Koukoulas and Blackburn (2000) developed a method for extracting the locations of treetops from LiDAR data and colour aerial photographs. Similarly, Popescu and Wynne (2004) fused LiDAR and 4-m multi-spectral Airborne Terrestrial Land Application Scanner (ATLAS) image data to improve estimates of individual tree height. They improved their average plot height estimation from LiDAR metrics by differentiating forest type from optical data. Methods for combining LiDAR-derived metrics and optical images have also been devised. Chen *et al.* (2004) used IKONOS, Landsat 7 ETM+ and LiDAR data to quantify coniferous forest and understorey grass coverage in a ponderosa pine forest. They compared optical-derived cover estimates of bare soil, understorey grass and tree/shade to similar cover estimates derived from LiDAR data, and found significant correlations (R^2 ranging from 0.58 to 0.79) between optical-derived tree/shade fractions and LiDAR-derived cover estimations. Lefsky *et al.* (2005b) proposed an approach to estimate aboveground net primary production based on stand age and biomass. Stand age was obtained by iterative unsupervised classification of multi-temporal Landsat TM images and aboveground biomass was estimated from LiDAR data. Productivity estimates from this approach compared well with forest inventory estimates. Donoghue and Watt (2006) compared predictions of forest height derived from LiDAR and from optical images (IKONOS and Landsat ETM+). Their study concluded that LiDAR data provided an accurate estimate of height ($R^2 = 0.98$) in very densely stocked Sitka spruce crops over the entire range of age classes studied. Nevertheless, the optical imagery generated accurate predictions of forest height only in the range 0–10 m; above 10 m height predictions were very poor. In addition, two coincident LiDAR transects, representing 1997 and 2002 forest conditions in the boreal forest of Canada, were compared using image segments generated from Landsat ETM+ imagery (Wulder *et al.* 2007). The image segments were used to provide a spatial framework within which the attributes and temporal dynamics of the forest canopy were estimated and compared.

However, very few studies have combined LiDAR-derived metrics and Landsat spectral indices in regression models. Wulder and Seemann (2003) developed regression models to relate Landsat 5 TM digital numbers (DNs) with quantile-based estimates of canopy top height derived from SLICER (Scanning LiDAR Imager of Canopies by Echo Recovery) data, in polygons and segments. Nevertheless, these authors did not combine different LiDAR-derived summaries and spectral indices or study correlation among both datasets, and they only obtained acceptable accuracy ($R^2 = 0.62$) for the segment approach.

Given the relationship between mean, median and variability of canopy height derived from LiDAR and forest structure (Pascual *et al*. 2008), the objective of the present work was to evaluate the relationship among mean, median, SD and coefficient of variation (CV) derived from LiDAR and Landsat spectral indices; that is, shortwave infrared (SWIR)-associated indices, Tasseled Cap, principal component analysis (PCA) and normalized difference indices. This would be a first step in proposing the future development of new support tools for forest management on a regional scale.

2. Materials and methods

2.1 *Study area*

A 127 ha (1293 m × 983 m) area, located on the western slopes of the Fuenfría Valley (40° 45′ N, 4° 5′ W) in central Spain, was selected as the study area. The Fuenfría Valley is located in the northwest portion of the Madrid region (see figure 1). The predominant forest is Scots pine (*Pinus sylvestris* L.) with abundant shrubs of *Cytisus scoparius* (L.) Link., *C. oromediterraneus* Rivas Mart. *et al.* and *Genista florida* (L.). On the lowest part of the hillside there are small pastures and there is an extensive rocky area in the north of the study site (see figure 2). This area was selected based on its representativeness within the pine forest of Fuenfría Valley, according to the opinion of local forest managers and based on our previous data from the research permanent plots network that we have in the area, as described in Pascual (2006) and Pascual *et al*. (2008).

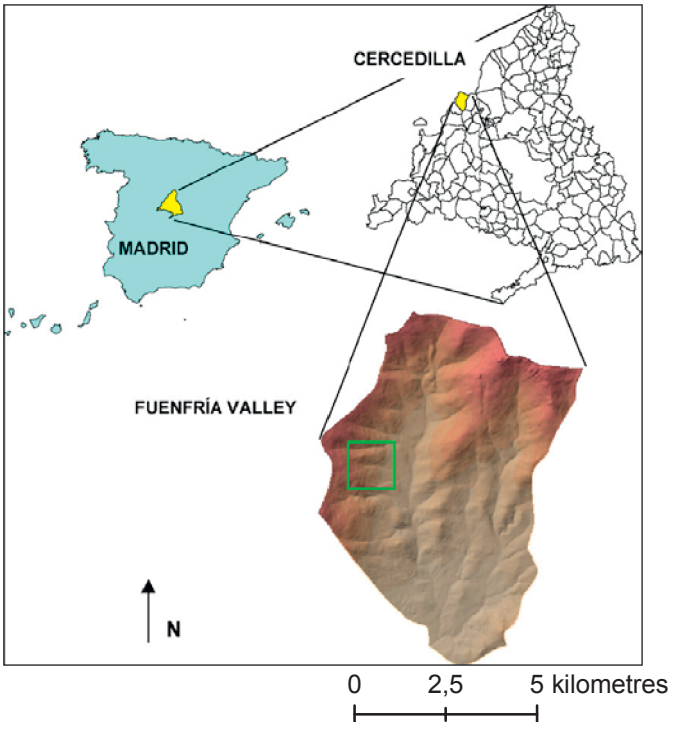

Figure 1. Study site. Fuenfría Valley, in the village of Cercedilla, northwest of Madrid (Spain).

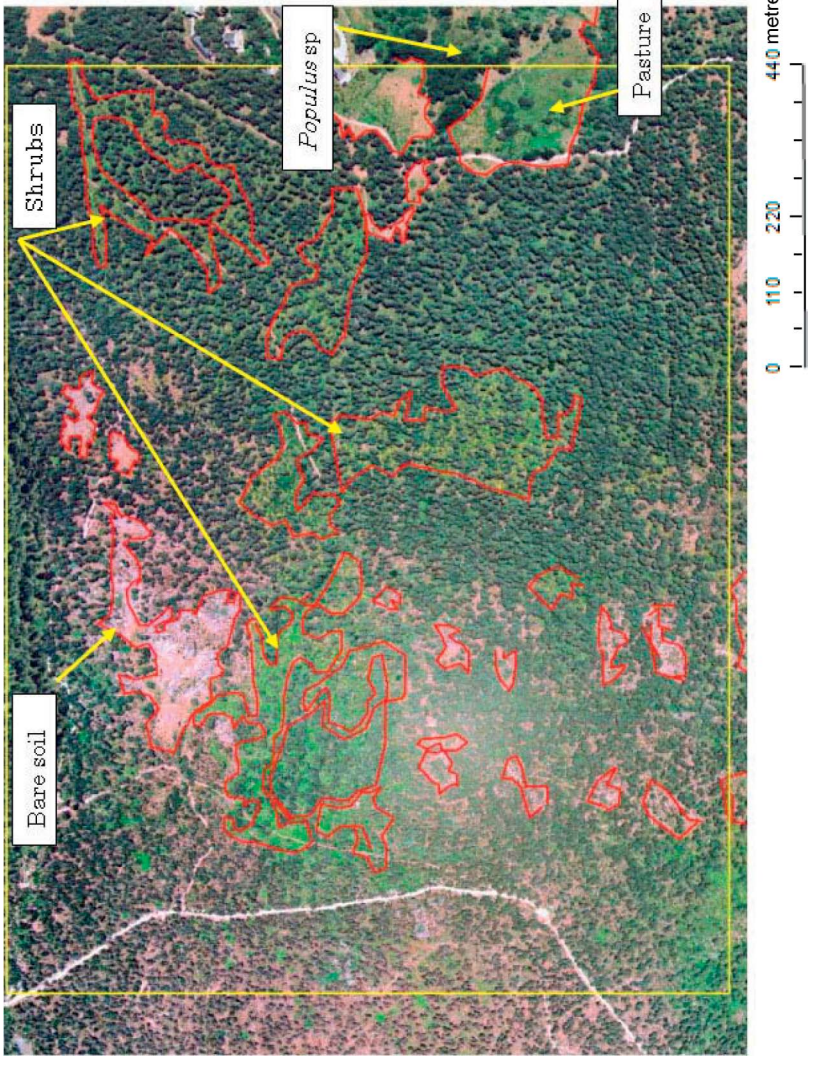

Figure 2. A 0.5-m pixel digital orthophotograph of the study area (yellow frame). Different cover types (pasture, bare soil, shrubs and *Populus* sp.) were digitized and labelled.

Elevations range between 1310 and 1790 m above sea level, with slopes between 20% and 45%. The general aspect of the study site is east. The site has a mean annual temperature of 9.4°C and precipitation averages 1180 mm year^{-1}.

2.2 *LiDAR data*

A small-footprint LiDAR dataset was acquired by TopoSys GmbH over the study area in August 2002. The TopoSys II LiDAR system recorded first and last returns with a footprint diameter of 0.95 m. Average point density was 5 points m^{-2}. The raw data (x, y, z-coordinates) were processed into a 1-m-pixel digital surface model (DSM) and 1-m-pixel digital terrain model (DTM) by TopoSys, using a local adaptive median filter developed by the data provider. The DSM was processed using the first returns and the DTM was constructed using the last returns. Filtering algorithms were used to identify canopy and ground surface returns for an output pixel resolution of 1 m horizontal and 0.1 m vertical resolution. According to Toposys calculations for the DSM and DTM, horizontal positional accuracy was 0.5 m and vertical accuracy was 0.15 m. To obtain a digital canopy height model (DCHM), the DTM was subtracted from the DSM. Both the DTM and DCHM were validated before use by land surveying using a total station in 19 points and ground-based tree height measurements of 102 trees. Vertical accuracies (i.e. root mean square error, RMSEs) obtained for the DTM in open areas and for the DCHM under forest canopy were 0.30 and 1.3 m, respectively. These accuracies were acceptable for this study, and were in agreement with previous studies (Clark *et al.* 2004).

2.3 *Image data and preprocessing*

Three Landsat ETM+ images from scene path/row (201/32) corresponding to three different dates (15 March 2000, 6 June 2001 and 10 September 2001) were georeferenced and radiometrically calibrated. The projection system was UTM (Datum European 1950) with a pixel resolution of 30 m.

The June and September Landsat images were previously co-registered using digital maps and a 50-m-pixel DTM. The RMSE of georegistration was < 1 pixel in both cases (Heredia-Laclaustra *et al.* 2003). We checked the co-registration accuracy using nine easily recognizable points. We orthorectified and adjusted the March image to the September image by setting a total of 38 ground control points (GCPs) over a 30 km $\times$ 30 km subset area centred on the study site. This area allowed the identification of a larger number of GCPs, ensuring the accuracy of the transformation for the study area. The RMSE of the transformation was 11.5 m (0.4 pixels). In addition, different forest cover patches were digitized from an aerial photograph (see figure 2) and served as reference for the registration of the different Landsat images.

The cosine estimation of atmospheric transmittance (COST) absolute radiometric correction model of Chavez (1996) was applied to each image to convert digital counts to reflectance. This model consists of a modification of the dark-object subtraction (DOS) method by including a simple multiplicative correction for the effect of atmospheric transmittance.

2.4 *LiDAR DCHM summaries and spectral indices*

The LiDAR DCHM (1 m pixel) was degraded to 30-m cell blocks providing a grid of 32 rows and 42 columns with 30-m cells. The mean, median, SD and CV of the 900 LiDAR height values contained inside each 30 m $\times$ 30 m block were calculated. Four

new 30-m-pixel images of mean (HMN), median (HMD), standard deviation (HSD) and coefficient of variation (HCV) of LiDAR height values were obtained.

Several near-infrared (NIR)- and SWIR-derived spectral measures were calculated for each Landsat image (see table 1). These indices, grouped into two categories, included: (1) normalized difference indices (the normalized difference vegetation index (NDVI), normalized difference moisture index (NDMI) and normalized burn ratio (NBR)) and (2) linear transform of multiple bands (Tasseled Cap (brightness, greenness, wetness) and unstandardized PCA). Tasseled Cap transformation was obtained using the coefficients for brightness, greenness and wetness derived by Huang *et al*. (2002) for Landsat ETM+ at reflectance data (see table 1).

2.5 *Sample design and statistical analysis*

Unsupervised classification of the September Landsat was performed to mask bare soil, rocks, pasture and shrubs from subsequent analysis and focus the statistical analysis over the pine forest cover.

In addition, a systematic sampling was used to reduce the spatial autocorrelation inherent in remote sensing imagery. The sampling procedure was designed based on semivariograms of the LiDAR DCHM mean height and Tasseled Cap wetness component of the three dates. Semivariograms were calculated using the free distribution software Variowin 2.2 (Pannatier 1996). Mean LiDAR height was selected based on the correlations with spectral indices found in previous work (Pascual 2006), and the Tasseled Cap wetness component was selected as this is related to forest structure (Cohen and Spies 1992). The semivariance tended to stability at 130–150 m. Two systematic samples were obtained: one for statistical model-building and the other to provide an independent validation of the model. For each sample we selected the 25 pixels (a window of 5×5 pixels) in the upper left corner of the image. The starting point of the model sample was randomly selected from this subsample of 25 pixels. From the starting pixel, we took every fifth pixel, or fourth pixel when the previous one was not possible. We developed this approach twice, once for the model sample and once to build the validation sample.

Pearson and Spearman correlations were carried out among the Landsat spectral indices and LiDAR statistical descriptors. Regression analyses were also carried out between both sets of variables. Finally, an independent validation served as a basis for comparing the ordinary least squares (OLS) regression method and the reduced major axis (RMA) regression method. OLS regression assumes that an independent variable X is measured without error and coefficients for the regression are calculated by minimizing the sum of square errors in Y (i.e. the dependent variable). In this case, estimates of slope are biased, with a resulting compression of the variance of predictions. In other words, values above the mean of Y tend to be underpredicted and values below the mean tend to be overpredicted. The RMA makes no assumptions about errors in X and Y. Therefore, this method minimizes the sum of squared orthogonal distances from measurement points to the model function. The effect of this is to minimize or eliminate any attenuation or amplification of predictions (Cohen *et al*. 2003). The RMA regression is defined by simple regression paradigms. Following the procedure of these authors, prior to RMA analysis, it was necessary to apply a canonical correlation analysis (CCA) to the body of predictive variables to integrate all independent variables in one spectral index.

Table 1. Spectral indices calculated with the Landsat data.

Vegetation indices	Formula
Normalized difference indices	
NDVI	$\frac{TM4 - TM3}{TM4 + TM3}$
NDMI	$\frac{TM4 - TM5}{TM4 + TM5}$
NBR	$\frac{TM4 - TM7}{TM4 + TM7}$
Image transformation	
Brightness	0.356 TM1 + 0.397 TM2 + 0.390 TM3 + 0.697 TM4 + 0.229 TM5 + 0.159 TM7
Greenness	–0.334 TM1 – 0.354 TM2 – 0.456 TM3 + 0.697 TM4 – 0.024 TM5 – 0.263 TM7
Wetness	0.263 TM1 + 0.214 TM2 + 0.093 TM3 + 0.066 TM4 – 0.763 TM5 – 0.539 TM7
PC1 March	0.108 TM1 + 0.163 TM2 + 0.232 TM3 + 0.363 TM4 + 0.868 TM5 + 0.150 TM7
PC2 March	0.028 TM1 + 0.047 TM2 – 0.002 TM3 + 0.912 TM4 – 0.402 TM5 + 0.053 TM7
PC3 March	–0.325 TM1 – 0.445 TM2 – 0.706 TM3 + 0.176 TM4 + 0.289 TM5 – 0.288 TM7
PC1 June	0.085 TM1 + 0.147 TM2 + 0.179 TM3 + 0.446 TM4 + 0.714 TM5 + 0.481 TM7
PC2 June	–0.053 TM1 – 0.045 TM2 – 0.156 TM3 + 0.884 TM4 – 0.268 TM5 – 0.342 TM7
PC3 June	–0.317 TM1 – 0.474 TM2 – 0.693 TM3 – 0.075 TM4 + 0.423 TM5 – 0.100 TM7
PC1 September	0.088 TM1 + 0.140 TM2 + 0.223 TM3 + 0.275 TM4 + 0.761 TM5 + 0.516 TM7
PC2 September	–0.048 TM1 – 0.034 TM2 – 0.125 TM3 + 0.948 TM4 – 0.118 TM5 – 0.260 TM7
PC3 September	–0.344 TM1 – 0.454 TM2 – 0.703 TM3 – 0.094 TM4 + 0.409 TM5 – 0.067 TM7

TM1, TM2, TM3, TM4, TM5 and TM7 are the reflectances of Landsat ETM+ for channels 1, 2, 3, 4, 5 and 7, respectively.

We conducted a statistical analysis to assess the relationship between the LiDAR height predictors and multi-temporal spectral measurements. Our aim was to understand the influence of multiple images versus a single image and the importance of different spectral vegetation indices and transformations. Two model-building approaches were used. The vegetation spectral indices NDVI, NDMI and NBR were considered from a single date, two dates and three dates. Spectral transformations (PCA and Tasseled Cap) of the three dates were also combined. Regarding the PCA, all possible combinations of the first three components (PC1, PC2 and PC3) were tested, with one, two or three dates. In addition, NDVI was combined with NDMI, NBR and wetness. This was done by building as many as 200 models, representing an exhaustive list of combinations of predictors (indices and dates). Regression analysis was constructed by a forward stepwise method (p enter = 0.05; p remove = 0.05). The Akaike Information Criterion (AIC; Quinn and Keough 2003) was calculated as an additional criterion for selecting the best models.

Statistical treatment was performed with the Statistica program version 6.1. Before proceeding with the analysis, the necessary transformations (i.e. logarithm and inversion of variables) were made to adjust the distributions of variables to the prerequisites required for statistical analysis. Normality was checked using the Shapiro–Wilks test.

3. Results

Sample plots of the 30-m-pixel images of LiDAR-derived metrics and of NDVI and Tasseled Cap components are shown in figures 3 and 4. Correlations between height descriptors from the LiDAR data and the spectral indices vary depending on variables

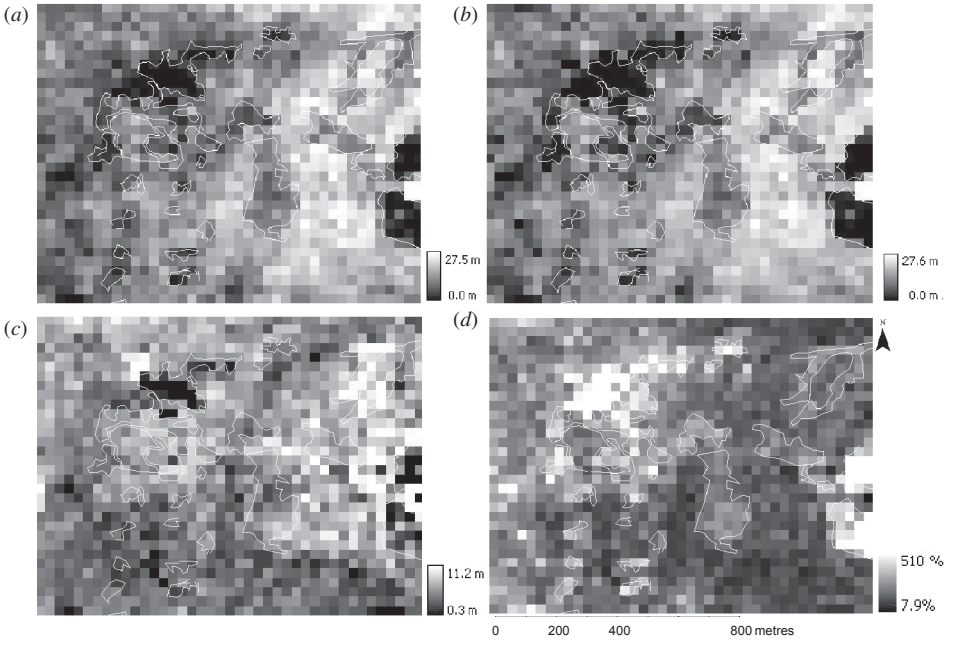

Figure 3. 30-m-pixel LiDAR-derived metrics images: (*a*) mean (HMN); (*b*) median (HMD); (*c*) standard deviation (HSD) and (*d*) coefficient of variation (HCV). Vectorial digitized cover types are included.

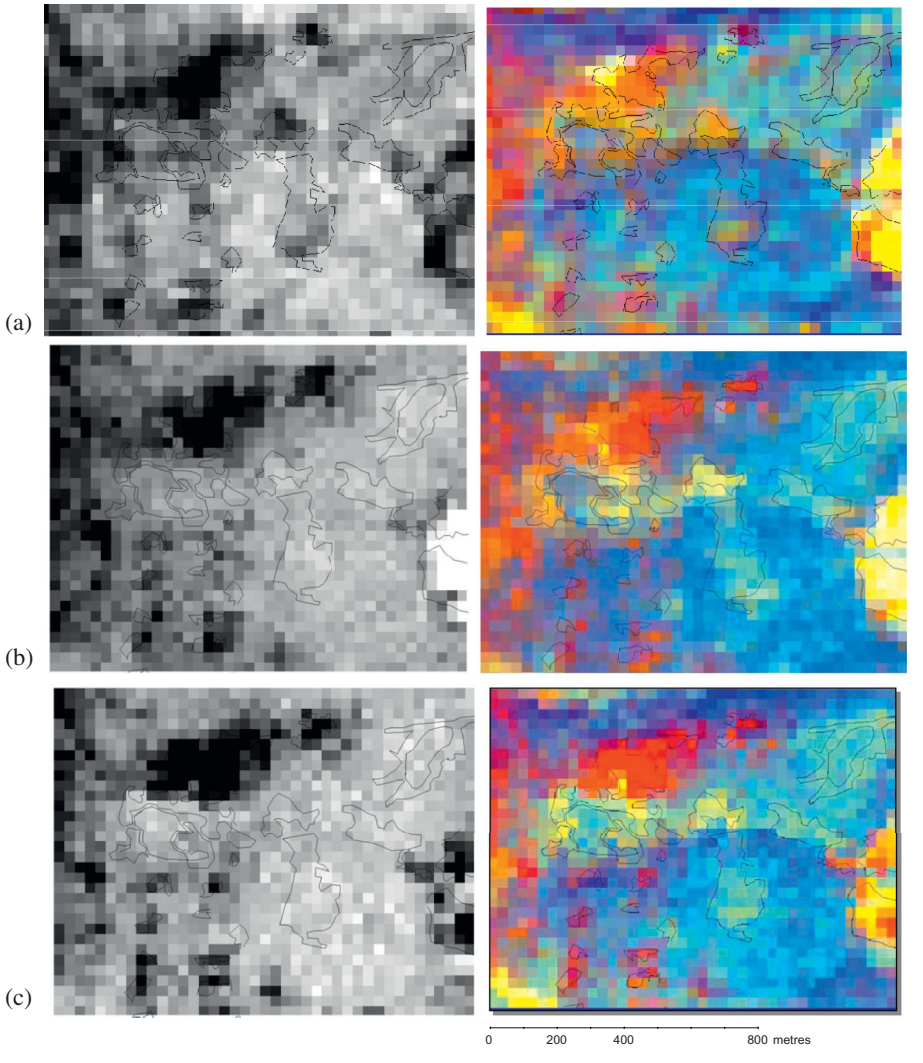

Figure 4. NDVI (left) and colour composition of the Tasseled Cap components (right): brightness in red channel; greenness in green channel and wetness in blue channel. (*a*) 15 March, (*b*) 6 June, and (*c*) 10 September with the feature digitized cover types (bare soil, pasture, shrubs).

and dates (see table 2). HMN and HMD show the highest correlation coefficients in all indices for the three dates, with mean height providing a slightly better relationship than the median LiDAR descriptor. HSD shows a non-significant relationship with all spectral variables from Landsat scenes for the three dates, and HCV shows an irregular pattern of behaviour (see table 2).

SWIR-derived indices (i.e. NDMI, NBR and wetness) show higher correlation coefficients with mean, median and CV LiDAR-derived height, with wetness showing a very slightly better relationship than the normalized differenced SWIR indices (NDMI and NBR). NDVI and PC1 of June and September also presented strong

Table 2. Correlation coefficients between spectral indices and LiDAR-derived metrics ($n = 46$).

Date		PC1	PC2	PC3	Br†	Gr	ln(–We)	NDVI	NDMI	NBR
March	HMN	–0.53*	0.62*	0.33**	–0.40*	0.61*	–0.59*	0.64**	0.67**	0.08
	HMD	–0.52*	0.64*	0.34**	–0.38*	0.63*	–0.59*	0.62**	0.64**	0.12
	HSD	–0.24	0.23	0.11	–0.16	0.24	–0.19	0.06	–0.06	–0.14
	HCV	0.45*	–0.53*	–0.37**	0.37**	–0.58*	0.55*	–0.61**	–0.61**	–0.18
June	HMN	–0.71*	0.66*	0.06	0.57*	0.67*	–0.74*	0.73**	0.69**	0.67**
	HMD	–0.71*	0.66*	0.06	0.57*	0.67*	–0.74*	0.73**	0.67**	0.66**
	HSD	–0.27	0.25	0.38*	0.16	0.37	–0.17	0.33**	–0.08	–0.03
	HCV	0.69*	–0.54*	0.16	–0.59*	–0.49**	0.72*	–0.52**	–0.63**	–0.59**
September	HMN	–0.70*	0.34**	–0.13	0.54*	0.54**	–0.76*	0.73**	0.75**	0.76**
	HMD	–0.68*	0.36**	–0.10	0.52*	0.54**	–0.75*	0.745**	0.73**	0.75**
	HSD	–0.23	0.15	0.28	0.19	0.29	–0.15	0.25	–0.18	–0.10
	HCV	0.65*	–0.33**	0.29	–0.48*	–0.46	0.74*	–0.58**	–0.77**	–0.74**

Br, Gr and We are brightness, greenness and wetness Tasseled Cap components derived from ETM+.
* Correlation significant at $p < 0.01$. ** Correlation significant at $p < 0.05$.
†Brightness components are Br for March and 1/Br for June and September.

correlations with LiDAR-derived summaries. Indices from March provided lower correlation coefficients than those of June or September.

Nearly all the possible combinations of spectral indices produced multiple regression models, with adjusted R^2 ranging from 0.150 to 0.695. In the present study, we have only considered those models with R^2 of ≥ 0.65. Ten, eight and one regression models were selected with HMN, HMD and HCV as the dependent variable, respectively (see table 3). HSD derived from LiDAR was excluded from the regression analysis because of low correlation coefficients (see table 2). All models verify the assumption of normality of the standard residuals according to the Shapiro–Wilks test, with a mean standard residual of zero in all the models. The Durbin–Watson statistic, D, was between −2 and 2 for all the models; therefore none of the models show correlation among their residuals. Finally, in all cases, Cook's distance was < 3, which is the threshold to detect outliers according to Quinn and Keough (2003).

Models including HMN and HMD as the dependent variable provided better adjusted R^2 than those containing HCV (see table 3). Selected HMN and HMD models included nearly the same spectral indices as predictors but HMN regressions provided slightly better accuracy according to the RMSE values. Most of the models include predictors of different dates, except for models 8 and 17, which only included NBR for September. According to R^2 adjusted and AIC values, most of the best models included three predictors from the three different dates (see model 16, table 3).

As expected, RMA regression in comparison with traditional OLS regression provides higher values for the slope (see table 4). Scatterplots of predicted versus observed for the OLS regression method show higher compression of the variance of predictions than those of the RMA (see figures 5 and 6).

4. Discussion

LiDAR data offer substantial improvements over other optical sensors of higher spectral resolution in the accuracy of predictions of forest structural attributes (Lefsky *et al*. 2001). Nevertheless, laser scanner data are economically and computationally constrained at broad regional scales (Sexton *et al*. 2009). Therefore, Landsat or other passive image data are required to extrapolate LiDAR height measurements across a broad landscape. We could use field-measured height instead of LiDAR-derived canopy height, but LiDAR provides many orders of magnitude more observations of height than field data. In addition, our results show that the mean height of the outer canopy derived from LiDAR (HMN) provides correlation coefficients with Landsat spectral indices that equal or improve the correlations between Landsat-derived indices and the mean height of individual trees (Cohen *et al*. 1995, Lu *et al*. 2004, Freitas *et al*. 2005).

Some authors have reported a strong correlation between SWIR bands and associated indices and multiple forest attributes (Cohen and Spies 1992, Cohen *et al*. 1995, Jakubauskas 1996, Steininger 2000, Lu *et al*. 2004, Freitas *et al.* 2005). In the present study, mean LiDAR-derived canopy height (HMN) and SWIR-derived indices (wetness, NDMI and NBR) show higher correlation coefficients than those reported in the literature for SWIR-derived indices and mean plot height in areas of simple forest structure (R ranging from 0.247 to 0.619) (Cohen *et al*. 1995, Lu *et al*. 2004, Freitas *et al*. 2005). However, in complex forest structures (multiple strata), Lu *et al*. (2004) and Freitas *et al*. (2005) reported higher correlation coefficients (R ranging from 0.785 to 0.908) among SWIR-derived indices and mean height of individual trees. In fact,

Table 3. Regression models obtained with $R^2 \geq 0.65$ ($n = 46$).

		ID	Model	R^2	Adjusted R^2	RMSE	AIC
Principal components	HMN	1	HMN = 0.525 PC2_M + 0.547 PC2_J – 0.260 PC1_S	0.71	0.70	1.88	63.00
		2	HMN = 0.558 PC2_M – 0.351 PC1_S + 0.399 PC2_S	0.69	0.67	1.95	66.21
		3	HMN = 0.545 PC2_M – 0.280 PC1_J + 0.603 PC2_J	0.68	0.66	1.98	67.61
Tasseled Cap		4	HMN = 15.902 + 0.271 Br_M + 0.652 Gr_J – 8.421 ln(–We_S)	0.69	0.67	1.96	65.78
		5	HMN = 16.054 + 0.471 Gr_M + 0.628 Gr_J – 5.026 ln(–We_S)	0.69	0.66	1.97	66.34
		6	HMN = 19.602 + 0.271 Br_M + 0.409 Gr_S – 9.408 ln(–We_S)	0.68	0.66	2.00	67.53
Normalized differences		7	HMN = 15.6443 NBR_M + 26.4139 NBR_S	0.68	0.68	1.94	64.99
		8	HMN = – 3.6856+ 26.2978 NBR_S	0.66	0.65	2.02	66.72
Mixed		9	HMN = 0.271 Br_M + 26.402 NDVI_J – 6.850 ln(–We_S)	0.70	0.69	1.91	64.36
		10	HMN = 30.056 NDVI_J – 4.134 ln(–We_S)	0.66	0.66	2.00	67.53
Principal components	HMD	11	HMD = 0.585 PC2_M + 0.573 PC2_J – 0.298 PC1_S	0.70	0.69	2.13	74.44
		12	HMD = 0.607 PC2_M – 0.397 PC1_S + 0.435 PC2_S	0.69	0.68	2.17	76.32
		13	HMD = 0.622 PC2_M – 0.330 PC1_J + 0.636 PC2_J	0.69	0.67	2.19	76.91
Tasseled Cap		14	HMD = 15.717 + 0.630 Gr_M + 0.716 Gr_J – 5.117 ln(–We_S)	0.68	0.66	2.24	78.05
		15	HMD = 19.619 + 0.323 Br_M + 0.510 Gr_S – 10.375 ln(–We_S)	0.67	0.65	2.27	79.28
Normalized differences		16	HMD = 20.693 NBR_M + 29.6901 NBR_S	0.69	0.68	2.15	74.52
		17	HMD = –4.8053+ 29.4074 NBR_S	0.65	0.64	2.29	78.04
Mixed		18	HMD = 32.718 NDVI_J – 4.656 ln(–We_S)	0.69	0.67	2.29	80.19
Tasseled Cap	HCV	19	HCV = –221.25 + 2675.08 1/Br_S + 72.469 ln(–We_S)	0.65	0.64	11.35	226.40

Br, Gr and We are brightness, greenness and wetness Tasseled Cap components derived from ETM+. M, J and S stand for March, June and September, respectively.

Table 4. Regression models in the validation. Scatterplots of observed versus predicted of the independent sample ($n = 52$). Slope (b) of the line observed versus predicted [Y(predicted) = $a + b\ X$(observed)] for OLS and RMA regression methods.

ID	Model	R^2	b in OLS	b in RMA
19	HCV = –221.25 + 2675.08 1/Br_S + 72.469 ln(–We_S)	0.66	0.64	0.81
10	HMN = 30.056 NDVI_J – 4.134 ln(–We_S)	0.62	0.75	0.78
1	HMN = 0.525 PC2_M + 0.547 PC2_J – 0.260 PC1_S	0.58	0.65	0.76
18	HMD = 32.718 NDVI_J – 4.656 ln(–We_S)	0.58	0.64	0.76
2	HMN = 0.558 PC2_M – 0.351 PC1_S + 0.399 PC2_S	0.58	0.63	0.76
11	HMD = 0.585 PC2_M + 0.573 PC2_J – 0.298 PC1_S	0.57	0.58	0.76
12	HMD = 0.607 PC2_M – 0.397 PC1_S + 0.435 PC2_S	0.57	0.58	0.76
9	HMN = 0.271 Br_M + 26.402 NDVI_J – 6.850 ln(–We_S)	0.53	0.73	0.73
4	HMN = 15.902 + 0.271 Br_M + 0.652 Gr_J – 8.421 ln(–We_S)	0.53	0.67	0.73
16	HMD = 20.693 NDBR_M + 29.6901 NDBR_S	0.52	0.68	0.72
3	HMN = 0.545 PC2_M – 0.280 PC1_J + 0.603 PC2_J	0.52	0.64	0.72
5	HMN = 16.054 + 0.471 Gr_M + 0.628 Gr_J – 5.026 ln(–We_S)	0.51	0.69	0.71
15	HMD = 19.619 + 0.323 Br_M + 0.510 Gr_S –10.375 ln(–We_S)	0.51	0.57	0.71
7	HMN = 15.6443 NDBR_M + 26.4139 NDBR_S	0.51	0.63	0.71
17	HMD = –4.8053+ 29.4074 NDBR_S	0.50	0.57	0.72
8	HMN = –3.6856+ 26.2978 NDBR_S	0.50	0.63	0.71
13	HMD = 0.622 PC2_M – 0.330 PC1_J + 0.636 PC2_J	0.49	0.59	0.70
6	HMN = 19.602 + 0.271 Br_M + 0.409 Gr_S – 9.408 ln(–We_S)	0.47	0.65	0.69
14	HMD = 15.717 + 0.630 Gr_M + 0.716 Gr_J – 5.117 ln(–We_S)	0.46	0.61	0.68

Br, Gr and We are brightness, greenness and wetness Tasseled Cap components derived from ETM+. M, J and S stand for March, June and September, respectively.

several authors have related SWIR reflectance to the structural maturity of the forest (Cohen and Spies 1992, Cohen *et al*. 1995, Freitas *et al*. 2005).

Regarding NIR reflectance, the application of NDVI to forest structure characterization has given conflicting results. Hall *et al*. (1995) and Franklin *et al*. (1997) do not consider this spectral index especially appropriate for the study of forest attributes because of the weak correlation shown with certain vegetation parameters. However, significant correlations with leaf area index (LAI) have been found in both boreal (Chen and Cihlar 1996) and coniferous forest (Gong *et al*. 1995). In the present study, the correlations between HMN and NDVI are clearly greater than those reported in

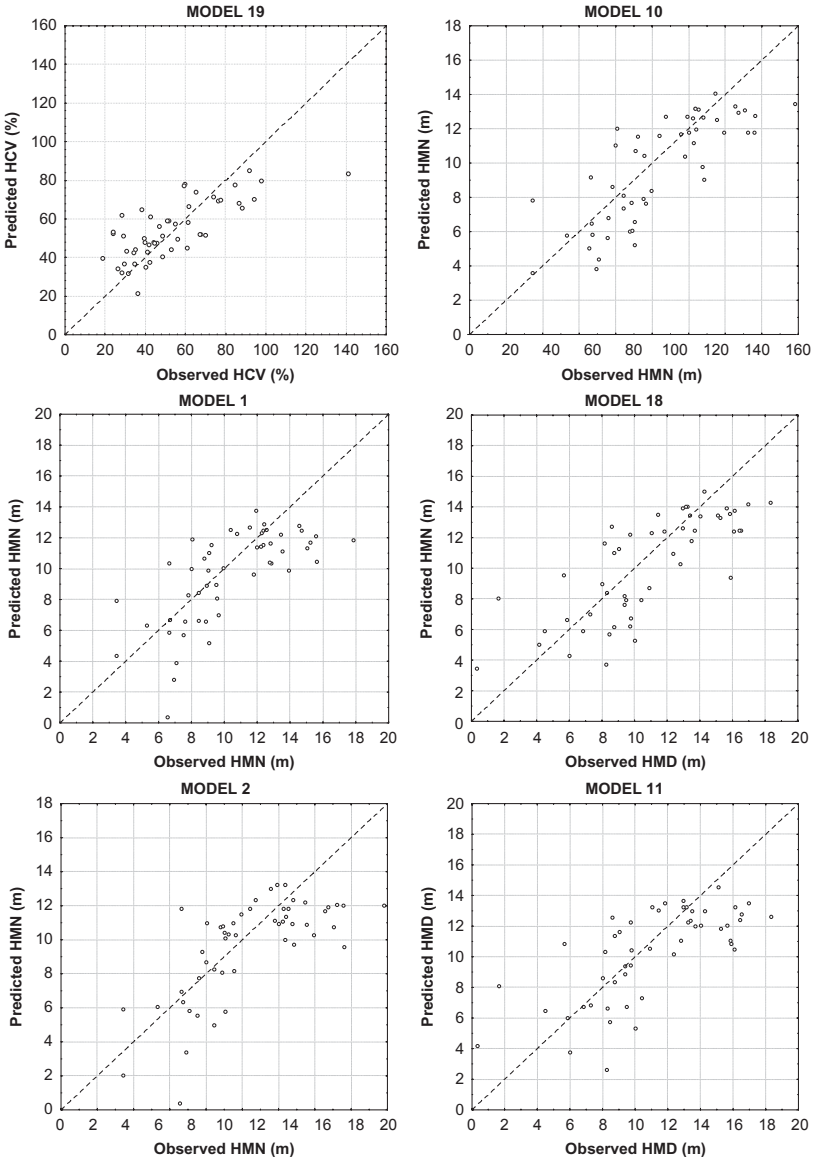

Figure 5. Scatterplot of observed versus predicted data for OLS regression models.

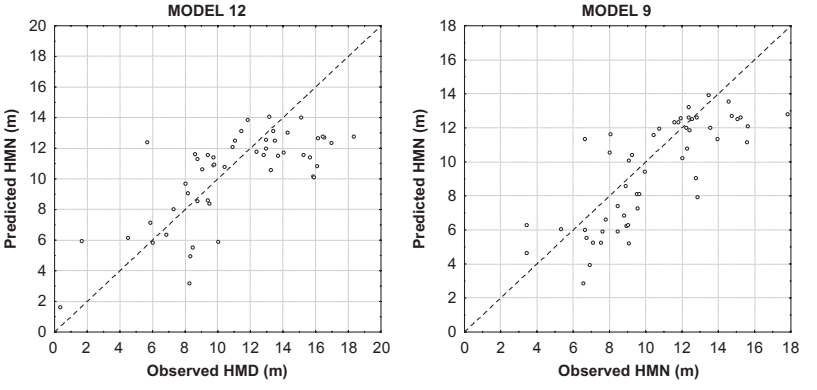

Figure 5. (*Continued.*)

the literature for field-derived mean height of individual trees. Indeed, the correlation coefficients between NDVI and mean field tree height range from 0.119 to 0.458 (Lu *et al*. 2004, Freitas *et al*. 2005) and exceptionally Lu *et al*. (2004) reported $R = 0.633$ in areas with a simple structure. This pattern has been considered as a constraint caused by the saturation of NDVI in very dense forest canopies (Freitas *et al*. 2005). These authors consider that, beyond a certain canopy density, the addition of more canopy layers makes little difference in the relative reflectance of red and NIR radiation and thus little difference in NDVI.

The literature indicates good correlations between mean height of individual trees and the SWIR reflectance in areas with a mature and complex structure, but very low correlations for the NDVI in these same areas of complex structure. However, our results for the mean height of the DCHM indicate very similar correlation values for all the spectral indices in heterogeneous Scots pine stands, although SWIR-derived index correlations are slightly stronger than NDVI. HMN correlates nearly equally strongly with SWIR-derived indices and NDVI because both are continuous variables related to the outer canopy that synthesize forest canopy information in 900 m^2.

Regarding multi-temporal issues, our results show that Landsat indices from March provided lower correlation coefficients with LiDAR-derived mean height of canopy than those of June or September. McDonald *et al*. (1998) found that vegetation indices were significantly affected by exogenous effects, including the solar zenith angle. In our latitude, the solar zenith angle and albedo might explain the lower correlations for March. In addition, according to Demarez *et al*. (1999), chlorophyll concentration in deciduous species increases during the first phase of the growing season (April) and stabilizes between June and September. In our Scots pine forest stands, this pattern might also describe the lower correlation coefficients for the spectral-derived indices of March. Nevertheless, canopy water content estimates appear to be independent of the cycle of photosynthetic activity in many plant communities (Trombetti *et al*. 2008).

The different spectral Landsat indices used in our study (see table 1) generated 10 regression models for HMN that have a similar R^2 (0.65–0.70). These results indicate the accuracy limit for the application of Landsat for use in large-scale multi-temporal studies of mean canopy height. This limit is partially due to Landsat's spatial

resolution, which has a 30 m pixel, and to the LiDAR-Landsat integration approach that degraded LiDAR data to coarser resolution. The accuracy of Landsat ETM+ georegistration was between 0.4 and 1 pixel, and therefore in some samples we may not have compared the spectral response with the matching LiDAR metrics. This is particularly significant in horizontally heterogeneous Scots pine stands and leads us to consider that the R^2 of the models are accurate.

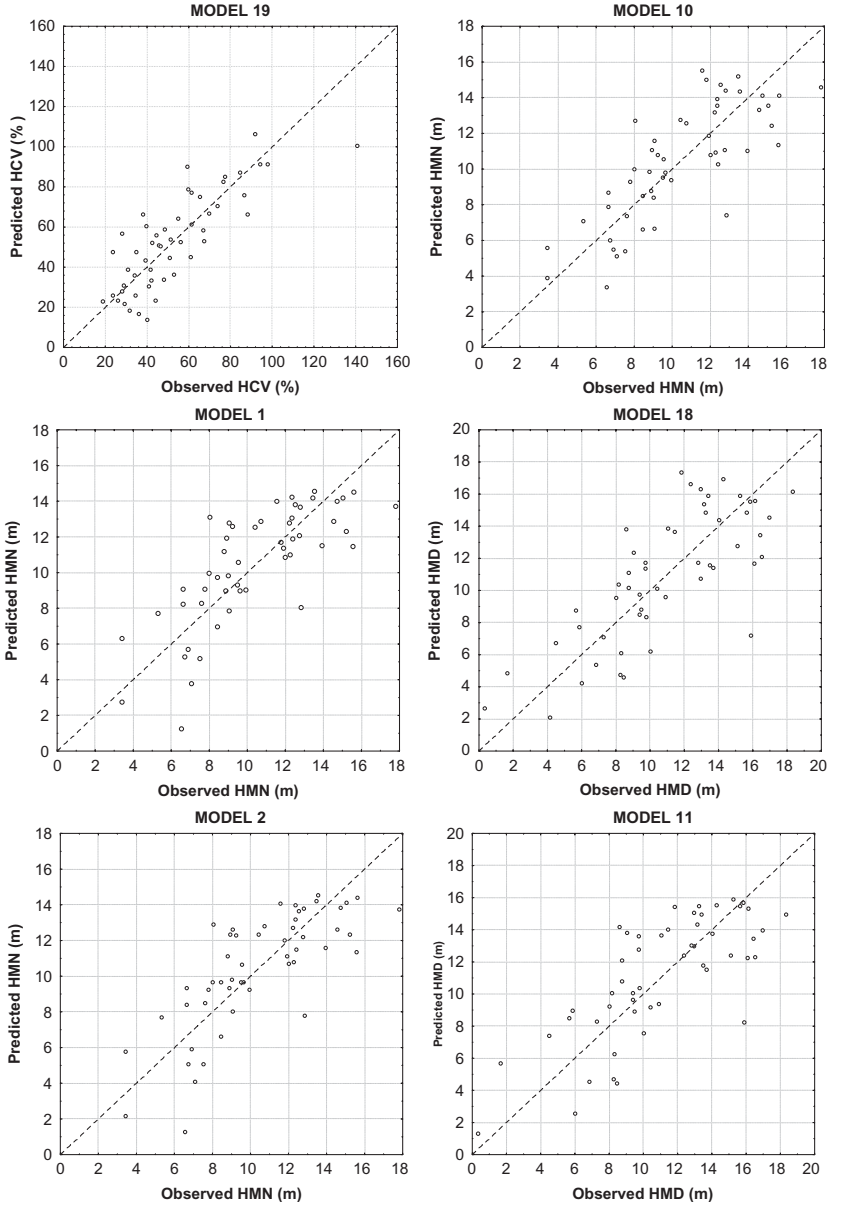

Figure 6. Scatterplot of observed versus predicted data for RMA regression models.

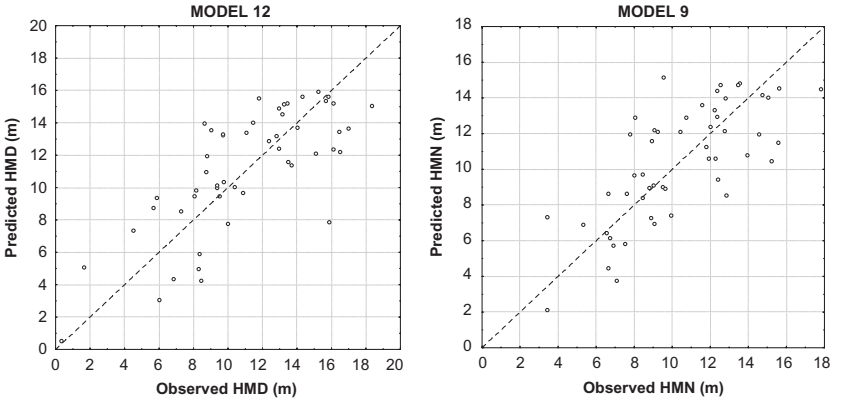

Figure 6. (*Continued.*)

Our results (see table 3) improve on previously published mean field tree height estimations as a function of wetness and NDMI (e.g. Cohen *et al*. 1995: $R^2 = 0.523$; Freitas *et al*. 2005: $R^2 = 0.559$). They also improve on maximum field tree height estimations based on multi-temporal Landsat information (Lefsky *et al*. 2001: $R^2 = 0.64$). Previous studies that relate waveform LiDAR-derived height and DNs of Landsat images have lower accuracies. Wulder and Seemann (2003) estimated LiDAR-derived height based on the DN values of image segments ($R^2 = 0.61$, RMSE = 4.06). Therefore, our results (see table 3) show an improved accuracy, especially for the standard error, when considering spectral indices instead of DN, and because of the different integration approach. The regression models of Hudak *et al*. (2002) explain a lower proportion of the total variation in canopy ($R^2 = 0.58$), although they developed several interesting spatial extrapolation methods for linking LiDAR data and Landsat bands.

According to the R^2 adjusted and AIC values, the best models included two or three predictors from different dates. These results are consistent with Lefsky *et al.* (2001), who consider that multi-temporal TM analysis improves forest attribute predictions. Scatterplots of observed versus predicted LiDAR height metrics (in the validation sample) (see figures 5 and 6) served as a basis for validating the models (see table 4). According to the validation results, the best models were based on PCA components. However, PCA is a statistical technique that is dataset dependent. Therefore, it is difficult to generalize the interpretation of PCA axes to other dataset. Moreover, unlike the Tasseled Cap, it is not possible in the PCA to give the resulting components an *a priori* significance (Cohen *et al.* 2003). All these reasons and the simplicity of the model led us to select model 10 as the best model.

The use of the DCHM has made it possible to obtain LiDAR-derived metrics (i.e. HMD and HCV), which are considered to synthesize information on forest structure (Zimble *et al*. 2003, Lefsky *et al*. 2005b, Pascual *et al.* 2008). HCV and HMD presented significant correlations (up to –0.75) and regression coefficients (adjusted from $R^2 = 0.64$ to 0.69) with Landsat-derived spectral indices. In our previous studies in the present study area, we have defined five structure types based on HMN, HMD and the SD of LiDAR height. These forest types range from high dense forest canopy (850 trees ha^{-1} and Lorey's height of 17.4 m) to scarce tree

coverage (60 tree ha^{-1} and Lorey's height of 9.7 m) (Pascual *et al.* 2008). For this classification, HMN and HMD of the five forest types differ by around 2.5 m on average. The accuracy of our regression models as indicated by the RMSE range from 1.9 to 2.3 m. These results suggest that improved accuracy might be required before applying these models to characterize forest structure in horizontally heterogeneous Scots pine stands in Fuenfría Valley. Our results point to an upper limit ($R^2 = 0.70$) of the explained variation in LiDAR-derived canopy height based on Landsat information due to the spatial resolution and co-registration of Landsat images. Therefore, further research involving smaller resolution imagery, careful co-registration of LiDAR-spectral datasets and stratification in homogeneous areas should be tested. In addition, RMA regression results (see figures 5 and 6), which are consistent with Cohen *et al.* (2003), encourage the use of this alternative procedure to improve the accuracy of LiDAR-derived summaries in forest structure studies.

4. Conclusions

LiDAR metrics are nearly equally strongly correlated to SWIR-associated indices (wetness, NDMI and NBR), NDVI and PC1. Estimations of LiDAR-derived summaries as a function of Landsat spectral indices improve mean field tree height estimations based on Landsat-derived indices. Although the results are from a relatively small area, they do show great promise for applicability to the larger area represented by the Fuenfría Valley, which consists of forests similar to those studied here. The present approach may be of interest in forest management plans using a small training LiDAR dataset combined with multi-temporal Landsat scenes. Nevertheless, the spatial resolution of Landsat imagery and co-registration with LiDAR data limit the accuracy of characterizing forest structure in horizontally heterogeneous Scots pine stands. Further research is required to apply this novel LiDAR–Landsat linking approach with higher resolution imagery and using the RMA regression.

Acknowledgements

Financial support for this study was provided by the Ministry of Industry, Tourism and Trade of Spanish Government through Project LINHE (FIT 330221-2006-10) and by the Technical University of Madrid (UPM) through Project CCG07-UPM/AMB-2056. We thank L. G. Garcia-Montero and R. Valbuena for their collaboration and suggestions, and the anonymous reviewers for their suggestions, Dr Ross Hill for his careful editing and P. Brooke-Turner for her assistance with the English.

References

Chavez, P., 1996, Image-based atmospheric corrections – revisited and improved. *Photogrammetric Engineering and Remote Sensing*, **62**, pp. 1025–1036.

Chen, J.M. and Cihlar, J., 1996, Retrieving leaf area index of boreal conifer forests using Landsat TM images. *Remote Sensing of Environment*, **55**, pp. 152–162.

Chen, X.X., Vierling, L., Rowell, E. and Defelice, T., 2004, Using lidar and effective LAI data to evaluate IKONOS and Landsat 7 ETM+ vegetation cover estimates in a ponderosa pine forest. *Remote Sensing of Environment*, **91**, pp. 14–26.

Clark, M.L., Clark, D.B. and Roberts, D.A., 2004, Small-footprint lidar estimation of subcanopy elevation and tree height in a tropical rain forest landscape. *Remote Sensing of Environment*, **91**, pp. 68–89.

COHEN, W.B., MAIERSPERGER, T.K., GOWER, S.T. and TURNER, D.P., 2003, An improved strategy for regression of biophysical variables and Landsat ETM+ data. *Remote Sensing of Environment*, **84**, pp. 561–571.

COHEN, W.B. and SPIES, T.A., 1992, Estimating structural attributes of Douglas-fir Western Hemlock forest stands from Landsat and Spot imagery. *Remote Sensing of Environment*, **41**, pp. 1–17.

COHEN, W.B., SPIES, T.A. and FIORELLA, M., 1995, Estimating the age and structure of forests in a multi-ownership landscape of Western Oregon, USA. *International Journal of Remote Sensing*, **16**, pp. 721–746.

CRIST, E.P. and CICONE, R.C., 1984, A physically-based transformation of thematic mapper data – the TM tasseled cap. *IEEE Transactions on Geoscience and Remote Sensing*, **22**, pp. 256–263.

DEMAREZ, V., GASTELLU-ETCHEGORRY, J.P., MOUGIN, E., MARTY, G., PROISY, C., DUFRÊNE, E. and LE DANTEC, V., 1999, Seasonal variation of leaf chlorophyll content of a temperate forest. Inversion of the PROSPECT model. *International Journal of Remote Sensing*, **20**, pp. 879–894.

DONOGHUE, D.N.M. and WATT, P.J., 2006, Using LiDAR to compare forest height estimates from IKONOS and Landsat ETM+ data in Sitka spruce plantation forests. *International Journal of Remote Sensing*, **27**, pp. 2161–2175.

FRANKLIN, J.F., SPIES, T.A., PELT, R.V., CAREY, A.B., THORNBURGH, D.A., BERG, D.R., LINDENMAYER, D.B., HARMON, M.E., KEETON, W.S., SHAW, D.C., BIBLE, K. and CHEN, J., 2002, Disturbances and structural development of natural forest ecosystems with silvicultural implications, using Douglas-fir forests as an example. *Forest Ecology and Management*, **155**, pp. 399–423.

FRANKLIN, S.E., LAVIGNE, M.B., DEULING, M.J., WULDER, M.A. and HUNT, E.R., 1997, Estimation of forest Leaf Area Index using remote sensing and GIS data for modelling net primary production. *International Journal of Remote Sensing*, **18**, pp. 3459–3471.

FREITAS, S.R., MELLO, M.C.S. and CRUZ, C.B.M., 2005, Relationships between forest structure and vegetation indices in Atlantic Rainforest. *Forest Ecology and Management*, **218**, pp. 353–362.

GONG, P., PU, R.L. and MILLER, J.R., 1995, Coniferous forest leaf-area index estimation along the Oregon transect using compact airborne spectrographic imager data. *Photogrammetric Engineering and Remote Sensing*, **61**, pp. 1107–1117.

HALL, F.G., SHIMABUKURO, Y.E. and HUEMMRICH, K.F., 1995, Remote-sensing of forest biophysical structure using mixture decomposition and geometric reflectance models. *Ecological Applications*, **5**, pp. 993–1013.

HEREDIA-LACRAUSTRA, A., MARTÍNEZ-SÁNCHEZ, S., QUINTERO, E., PIREÑOS, W. and CHUVIECO, E., 2003, Comparison of different digital analysis techniques for mapping burnt areas using Landsat ETM+ [in Spanish]. *GeoFocus*, **3**, pp. 216–234.

HUANG, C., WYLIE, B., YANG, L., HOMER C. and ZYLSTRA, G., 2002, Derivation of a tasselled cap transformation based on Landsat 7 at-satellite reflectance. *International Journal of Remote Sensing*, **23**, pp. 1741–1748.

HUDAK, A.T., LEFSKY, M.A., COHEN, W.B. and BERTERRETCHE, M., 2002, Integration of lidar and Landsat ETM plus data for estimating and mapping forest canopy height. *Remote Sensing of Environment*, **82**, pp. 397–416.

HYYPPA, J., HYYPPA, H., LECKIE, D., GOUGEON, F., YU, X. and MALTAMO, M., 2008, Review of methods of small-footprint airborne laser scanning for extracting forest inventory data in boreal forests. *International Journal of Remote Sensing*, **29**, pp. 1339–1366.

JAKUBAUSKAS, M.E., 1996, Canonical correlation analysis of coniferous forest spectral and biotic relations. *International Journal of Remote Sensing*, **17**, pp. 2323–2332.

KOUKOULAS, S and BLACKBURN, G.A., 2000, Mapping individual tree location, height and species in broadleaved deciduous forest using airborne LIDAR and multi-spectral remotely sensed data. *International Journal of Remote Sensing*, **27**, pp. 431–455.

Lefsky, M.A., Cohen, W.B., Parker, G.G. and Harding, D.J., 2002, Lidar remote sensing for ecosystem studies. *Bioscience*, **52**, pp. 19–30.

Lefsky, M.A., Cohen, W.B. and Spies, T.A., 2001, An evaluation of alternate remote sensing products for forest inventory, monitoring, and mapping of Douglas-fir forests in western Oregon. *Canadian Journal of Forest Research*, **31**, pp. 78–87.

Lefsky, M.A., Hudak, A.T., Cohen, W.B. and Acker, S.A., 2005a, Geographic variability in lidar predictions of forest stand structure in the Pacific Northwest. *Remote Sensing of Environment*, **95**, pp. 532–548.

Lefsky, M.A., Hudak, A.T., Cohen, W.B. and Acker, S.A., 2005b, Patterns of covariance between forest stand and canopy structure in the Pacific Northwest. *Remote Sensing of Environment*, **95**, pp. 517–531.

Lu, D., Mausel, P., Brondizio, E. and Moran, E., 2004, Relationship between forest stand parameters and Landsat TM spectral responses in the Brazilian Amazon Basin. *Forest Ecology and Management*, **198**, pp. 149–167.

McDonald, A.J., Gemmell, F.M. and Lewis, P.E., 1998, Investigation of the utility of spectral vegetation indices for determining information on coniferous forests. *Remote Sensing of Environment*, **66**, pp. 250–272.

Pannatier, Y. (Ed.), 1996, *Variowin: Software for Spatial Data Analysis in 2D*. (New York: Springer-Verlag).

Pascual, C., 2006, Forest structure analysis using remote sensing: LiDAR (Light Detection and Ranging) and satellite imagery [in Spanish]. PhD thesis, Technical University of Madrid (UPM), Spain.

Pascual, C., Garcia-Abril, A., Garcia-Montero, L.G., Martin-Fernandez, S. and Cohen, W.B., 2008, Object-based semi-automatic approach for forest structure characterization using lidar data in heterogeneous *Pinus sylvestris* stands. *Forest Ecology and Management*, **255**, pp. 3677–3685.

Popescu, S.C. and Wynne, R.H., 2004, Seeing the trees in the forest: using Lidar and multispectral data fusion with local filtering and variable window size for estimating tree height. *Photogrammetric Engineering and Remote Sensing*, **70**, pp. 589–604.

Quinn, G.P. and Keough, M.J. (Eds), 2003, *Experimental Design and Data Analysis for Biologists*, pp. 137–140 (Cambridge: Cambridge University Press).

Sexton, J.O., Bax, T., Siqueira, P., Swenson, J.J. and Hensley, S., 2009, A comparison of lidar, radar, and field measurements of canopy height in pine and hardwood forest of southeastern North America. *Forest Ecology and Management*, **257**, pp. 1136–1147.

Steininger, M.K., 2000, Satellite estimation of tropical secondary forest above-ground biomass: data from Brazil and Bolivia. *International Journal of Remote Sensing*, **21**, pp. 1139–1157.

Trombetti, M., Riaño, D., Rubio, M.A., Cheng, Y.B. and Ustin, S.L., 2008, Multi-temporal vegetation canopy water content retrieval and interpretation using artificial neural networks of the continental USA. *Remote Sensing of Environment*, **112**, pp. 203–215.

Wulder, M. and Seemann, D., 2003, Forest inventory height update through the fusion of lidar data with segmented Landsat imagery. *Canadian Journal of Remote Sensing*, **29**, pp. 536–543.

Wulder, M.A., Han, T., White, J.C., Sweda, T. and Tsuzuki, H., 2007, Integrating profiling LIDAR with Landsat data for regional boreal forest canopy attribute estimation and change characterization. *Remote Sensing of Environment*, **110**, pp. 123–137.

Zimble, D.A., Evans, D.L., Carlson, G.C., Parker, R.C., Grado, S.C. and Gerard, P.D., 2003, Characterizing vertical forest structure using small-footprint airborne LiDAR. *Remote Sensing of Environment*, **87**, pp. 171–182.